arXiv:1611.01863v1 [astro-ph.HE] 7 Nov 2016

Deeper H.E.S.S. Observations of Vela Junior (RX J0852.0−4622): Morphology Studies and Resolved Spectroscopy

H.E.S.S. Collaboration, H. Abdalla[1], A. Abramowski[2], F. Aharonian[3,4,5], F. Ait Benkhali[3], A.G. Akhperjanian[†6,5], T. Andersson[10], E.O. Angüner[21], M. Arakawa[43], M. Arrieta[15], P. Aubert[24], M. Backes[8], A. Balzer[9], M. Barnard[1], Y. Becherini[10], J. Becker Tjus[11], D. Berge[12], S. Bernhard[13], K. Bernlöhr[3], R. Blackwell[14], M. Böttcher[1], C. Boisson[15], J. Bolmont[16], P. Bordas[3], J. Bregeon[17], F. Brun[26], P. Brun[18], M. Bryan[9], M. Büchele[36], T. Bulik[19], M. Capasso[29], J. Carr[20], S. Casanova[21,3], M. Cerruti[16], N. Chakraborty[3], R. Chalme-Calvet[16], R.C.G. Chaves[17,22], A. Chen[23], J. Chevalier[24], M. Chrétien[16], M. Coffaro[29], S. Colafrancesco[23], G. Cologna[25], B. Condon[26], J. Conrad[27,28], Y. Cui[29], I.D. Davids[1,8], J. Decock[18], B. Degrange[30], C. Deil[3], J. Devin[17], P. deWilt[14], L. Dirson[2], A. Djannati-Ataï[31], W. Domainko[3], A. Donath[3], L.O'C. Drury[4], K. Dutson[33], J. Dyks[34], T. Edwards[3], K. Egberts[35], P. Eger[3], J.-P. Ernenwein[20], S. Eschbach[36], C. Farnier[27,10], S. Fegan[30], M.V. Fernandes[2], A. Fiasson[24], G. Fontaine[30], A. Förster[3], S. Funk[36], M. Füßling[37], S. Gabici[31], M. Gajdus[7], Y.A. Gallant[17], T. Garrigoux[1], G. Giavitto[37], B. Giebels[30], J.F. Glicenstein[18], D. Gottschall[29], A. Goyal[38], M.-H. Grondin[26], J. Hahn[3], M. Haupt[37], J. Hawkes[14], G. Heinzelmann[2], G. Henri[32], G. Hermann[3], O. Hervet[15,45], J.A. Hinton[3], W. Hofmann[3], C. Hoischen[35], M. Holler[30], D. Horns[2], A. Ivascenko[1], H. Iwasaki[43], A. Jacholkowska[16], M. Jamrozy[38], M. Janiak[34], D. Jankowsky[36], F. Jankowsky[25], M. Jingo[23], T. Jogler[36], L. Jouvin[31], I. Jung-Richardt[36], M.A. Kastendieck[2], K. Katarzyński[39], M. Katsuragawa[44], U. Katz[36], D. Kerszberg[16], D. Khangulyan[43], B. Khélifi[31], M. Kieffer[16], J. King[3], S. Klepser[37], D. Klochkov[29], W. Kluźniak[34], D. Kolitzus[13], Nu. Komin[*23], K. Kosack[18], S. Krakau[11], M. Kraus[36], P.P. Krüger[1], H. Laffon[26], G. Lamanna[24], J. Lau[14], J.-P. Lees[24], J. Lefaucheur[15], V. Lefranc[18], A. Lemière[31], M. Lemoine-Goumard[26], J.-P. Lenain[16], E. Leser[35], T. Lohse[7], M. Lorentz[18], R. Liu[3], R. López-Coto[3], I. Lypova[37], V. Marandon[3], A. Marcowith[17], C. Mariaud[30], R. Marx[3], G. Maurin[24], N. Maxted[14], M. Mayer[7], P.J. Meintjes[40], M. Meyer[27], A.M.W. Mitchell[3], R. Moderski[34], M. Mohamed[25], L. Mohrmann[36], K. Morå[27], E. Moulin[18], T. Murach[7], S. Nakashima[44], M. de Naurois[30], F. Niederwanger[13], J. Niemiec[21], L. Oakes[7], P. O'Brien[33], H. Odaka[44], S. Öttl[13], S. Ohm[37], M. Ostrowski[38], I. Oya[37], M. Padovani[17], M. Panter[3], R.D. Parsons[3], N.W. Pekeur[1], G. Pelletier[32], C. Perennes[16], P.-O. Petrucci[32], B. Peyaud[18], Q. Piel[24], S. Pita[31], H. Poon[3], D. Prokhorov[10], H. Prokoph[10], G. Pühlhofer[29], M. Punch[31,10], A. Quirrenbach[25], S. Raab[36], A. Reimer[13], O. Reimer[13], M. Renaud[17], R. de los Reyes[3], S. Richter[1], F. Rieger[3,41], C. Romoli[4], G. Rowell[14], B. Rudak[34], C.B. Rulten[15], V. Sahakian[6,5], S. Saito[43], D. Salek[42], D.A. Sanchez[24], A. Santangelo[29], M. Sasaki[29], R. Schlickeiser[11], F. Schüssler[18], A. Schulz[37], U. Schwanke[*7], S. Schwemmer[25], M. Seglar-Arroyo[18], M. Settimo[16], A.S. Seyffert[1], N. Shafi[23], I. Shilon[36], R. Simoni[9], H. Sol[15], F. Spanier[1], G. Spengler[27], F. Spies[2], Ł. Stawarz[38], R. Steenkamp[8], C. Stegmann[35,37], K. Stycz[37], I. Sushch[*1], T. Takahashi[44], J.-P. Tavernet[16], T. Tavernier[31], A.M. Taylor[4], R. Terrier[31], L. Tibaldo[3], D. Tiziani[36], M. Tluczykont[2], C. Trichard[20], N. Tsuji[43], R. Tuffs[3], Y. Uchiyama[43], D.J. van der Walt[1], C. van Eldik[36], C. van Rensburg[1], B. van Soelen[40], G. Vasileiadis[17], J. Veh[36], C. Venter[1], A. Viana[3], P. Vincent[16], J. Vink[9], F. Voisin[14], H.J. Völk[3], T. Vuillaume[24], Z. Wadiasingh[1], S.J. Wagner[25], P. Wagner[7], R.M. Wagner[27], R. White[3], A. Wierzcholska[21], P. Willmann[36], A. Wörnlein[36], D. Wouters[18], R. Yang[3], V. Zabalza[33], D. Zaborov[30], M. Zacharias[25], R. Zanin[3], A.A. Zdziarski[34], A. Zech[15], F. Zefi[30], A. Ziegler[36], and N. Żywucka[38]

(Affiliations can be found after the references)

ABSTRACT

Aims. The γ-ray emission from the shell-type supernova remnant (SNR) RX J0852.0−4622 is studied in order to better characterize its spectral properties and its distribution over the SNR.

Methods. The analysis of an extended H.E.S.S. data set at very-high energies ($E > 100$ GeV) permits detailed studies of the morphology and the spectrum of the whole RX J0852.0−4622 region, as well as spatially-resolved spectroscopy. The H.E.S.S. data are combined with archival data from other wavebands and interpreted in the framework of leptonic and hadronic models. The joint *Fermi*-LAT-H.E.S.S. spectrum allows the direct determination of the spectral characteristics of the parent particle population in leptonic and hadronic scenarios using only GeV-TeV data.

Results. An updated analysis of the H.E.S.S. data shows that the spectrum of the entire SNR connects smoothly to the high-energy spectrum measured by *Fermi*-LAT. The increased data set makes it possible to demonstrate that the H.E.S.S. spectrum deviates significantly from a power law and is well described by both a curved power law and a power law with an exponential cut-off at an energy of $E_{cut} = (6.7 \pm 1.2_{stat} \pm 1.2_{syst})$ TeV. The joint *Fermi*-LAT-H.E.S.S. spectrum allows the unambiguous identification of the spectral shape as a power law with an exponential cut-off. No significant evidence is found for a variation of the spectral parameters across the SNR, suggesting similar conditions of particle acceleration across the remnant. A simple modeling using one particle population to model the SNR emission demonstrates that both leptonic and hadronic emission scenarios remain plausible. It is also shown that at least a part of the shell emission is likely due to the presence of a pulsar wind nebula around PSR J0855−4644.

Key words. γ-rays: observations – RX J0852.0−4622 – supernova remnants – PSR J0855−4644 – pulsar wind nebulae

1. Introduction

RX J0852.0−4622 (listed in Green's supernova remnant (SNR) catalog (Green 2009) as SNR G266.2−1.2, as HESS J0852−463

in the H.E.S.S. catalog[1], and commonly referred to as *Vela Junior*) belongs to the class of young shell-type SNRs that display broadband non-thermal emission and have been detected at very-high energies (photon energies $E > 100\,\mathrm{GeV}$; Katagiri et al. 2005; Aharonian et al. 2005, 2007). Its properties are similar to RX J1713.7−3946 (H.E.S.S. Collaboration et al. 2016a) and, like this object, it has been extensively studied at multiple wavelengths (for an overview see Aharonian et al. 2007). The distance to the remnant and its age are still under debate in the literature but the range of possible values is narrowing. Studies of the shell expansion in X-rays, based on *XMM-Newton* data and the assumption of a shock velocity of 3000 km/s, have established a distance of $\sim 750\,\mathrm{pc}$ and an age between 1700 yr and 4300 yr (Katsuda et al. 2008). Similar studies were also recently conducted with *Chandra* data from the years 2003 to 2008, placing a lower limit on the distance to the remnant at 500 pc (Allen et al. 2015). An upper limit is determined by the comparison of the detected $^{44}\mathrm{Ti}$ line emission with evolution models for different types of supernova (SN) explosions, yielding a highest allowed distance of 1 kpc (Iyudin et al. 2010). The distance estimate by Katsuda et al. (2008) is in the middle of the range of allowed values and is adopted hereafter.

The γ-ray emission from RX J0852.0−4622 has been interpreted in the framework of both hadronic (proton-proton interactions with subsequent π^0-decay) and leptonic (inverse Compton (IC) scattering of relativistic electrons on ambient radiation fields) scenarios, without a definite answer so far. The high magnetic fields implied by hadronic scenarios are supported by the existence of sharp filamentary X-ray structures in the northwestern (NW) rim of the remnant which have been resolved by *Chandra* (Bamba et al. 2005). The small effective width of these structures is explained by fast synchrotron cooling of relativistic electrons implying strong magnetic field amplification. The estimates of the amplified magnetic field strength range from $\gtrsim 100\,\mu\mathrm{G}$ (Berezhko et al. 2009) to $\sim 500\,\mu\mathrm{G}$ (Bamba et al. 2005). A softening of the X-ray spectrum of the remnant towards the interior of the SNR recently detected in the NW rim of RX J0852.0−4622 with *XMM-Newton* was interpreted as the gradual decrease of the cut-off energy of the electron spectrum due to fast synchrotron cooling (Kishishita et al. 2013). The authors show that the detected softening can be reproduced for a low magnetic field of a few $\mu\mathrm{G}$ which would, however, require a high value of the electron cut-off energy of $\sim 100\,\mathrm{TeV}$ near the shock front. For a lower value of the cut-off energy of about 20 TeV, a high magnetic field of $\gtrsim 100\,\mu\mathrm{G}$ is required, still suggesting a strong magnetic field amplification in the rim. Alternatively, the sharp X-ray filaments can be explained by non-linear damping of strong magnetic turbulence downstream the shock, which creates thin regions with an enhanced magnetic field strength (see e.g. Pohl et al. 2005). In this case the width of the filaments is limited by the extent of the regions with strong magnetic fields and the softening of the spectrum can be explained by the spatial variation of the magnetic field strength (Pohl et al. 2005; Rettig & Pohl 2012).

On the other hand, the hadronic scenario requires a relatively high density of the ambient medium of about $\sim 1\,\mathrm{cm}^{-3}$ (Aharonian et al. 2007) which is in contradiction with the lack of detected thermal X-ray emission. The lack of thermal emission places an upper limit on the ambient density at $\sim 0.01\,\mathrm{cm}^{-3}$ (Slane et al. 2001). Such a low density of the ambient medium is actually expected in the case of a core collapse SN explosion when the SNR is expanding inside the stellar bubble of

the progenitor star. This scenario is argued to be the case for RX J0852.0−4622, as supported by the detection of the central compact object (CCO) AX J0851.9−4617.4[2] close to the center of the remnant (Aschenbach 1998; Aschenbach et al. 1999; Slane et al. 2001). However, no pulsations were detected from the CCO and, moreover, later it was suggested that the source might be an unrelated planetary nebula (Reynoso et al. 2006). An ambient density as low as $0.01\,\mathrm{cm}^{-3}$ leads to an unrealistically high value of the total energy in protons of $\sim 10^{51}$ erg in the hadronic scenario (Tanaka et al. 2011). This would imply that all the energy from the SN explosion ($\sim 10^{51}$ erg) is used in accelerating particles, whereas normally this number is expected to be a factor ~ 10 lower. Several explanations were suggested to overcome the problem of inconsistency of the hadronic model with the lack of thermal X-ray emission. Telezhinsky (2009) suggested that RX J0852.0−4622 might be older (17500 yr) than usually assumed which would place it in the transition phase between the adiabatic and radiative phases of SNR evolution. In this case the expected thermal X-ray flux decreases due to the formation of the dense shell and the cooling of the gas. It should be noted here that the lack of thermal emission can be claimed only for the gas with a temperature above 1 keV, because at lower energies RX J0852.0−4622 is completely obscured by the strong thermal emission from the Vela SNR. Another possible explanation was suggested by Inoue et al. (2012) and later by Gabici & Aharonian (2014) for the RX J1713.7−3946 SNR showing that a highly inhomogeneous clumpy environment significantly increases the expected γ-ray emission from hadronic interactions, while the thermal X-ray emission might remain at a very low level because denser cores of gas in clumps, which carry most of the mass, can survive the shock passing without being ionized. The environment of RX J0852.0−4622 exhibits a number of large clouds of atomic hydrogen which are close to the current position of the main shock and coincident with the regions of enhanced emission from the remnant (see Obergaulinger et al. 2014, and references therein). The lack of thermal X-ray emission is at the same time a strong argument in favor of a leptonic scenario. The leptonic scenario is able to match the broadband emission from RX J0852.0−4622 suggesting, however, a very low average magnetic field of about $5 - 10\,\mu\mathrm{G}$ (Lee et al. 2013; Aharonian et al. 2007), which, in turn, seems to be in contradiction with the sharp filamentary structures detected in X-rays. Recent X-ray observations with *Suzaku* (Takeda et al. 2016) reveal a faint hard X-ray component in the NW rim of RX J0852.0−4622. X-rays are reported with a spectral index of $3.15^{+1.18}_{-1.14}$ in the energy range from 12 keV to 22 keV. The absence of roll-off in the X-ray spectrum disfavors one-zone synchrotron models with electron spectra in the form of a power law with an exponential cut-off. However, the uncertainties on the spectral parameters are too large to draw strong conclusions.

X-ray observations with *XMM-Newton* (Acero et al. 2013) led to the discovery of a pulsar wind nebula (PWN) with an extension of 150 arcsec around the energetic ($\dot{E} = 1.1\,10^{36}$ erg/s) radio pulsar PSR J0855−4644 that coincides with the shell of RX J0852.0−4622. The pulsar is energetic enough to power a very high energy PWN detectable by current-generation Cherenkov telescopes (H.E.S.S. Collaboration et al. 2016b). Measurements of the column density towards the pulsar and RX J0852.0−4622 in X-rays using *XMM-Newton* data show that both objects are located at similar distances. Nevertheless, an association of PSR J0855−4644 with the SNR seems unlikely due to the age difference (the pulsar characteristic age is 140 kyr) and

---

[1] https://www.mpi-hd.mpg.de/hfm/HESS/pages/home/sources/

[2] Also known as CXOU J085201.4−461753

the large speed (∼ 3000 km/s) needed by the pulsar in order to travel from the geometrical center of the SNR to its current position.

This paper reports new H.E.S.S. observations of RX J0852.0−4622. Section 2 describes the data set and the applied analysis techniques, and Sect. 3 presents the results of the conducted morphological and spectral studies. The results are discussed in the context of multiwavelength data and of a simple modeling using one particle population for the entire SNR emission in Sect. 4.

2. H.E.S.S. Observations and Data Analysis

H.E.S.S. is an array of five Cherenkov telescopes situated in the Khomas Highland of Namibia at an altitude of 1800 m above sea level. In its initial phase, it consisted of four 13 m diameter telescopes sensitive in the energy range of 100 GeV to 100 TeV. In 2012, a fifth, 28 m telescope was added at the center of the array that allows lowering the threshold of the instrument to several tens of GeV. All data presented in this work were taken in the initial phase of H.E.S.S. when only the 13 m telescopes were available. More details on the performance of H.E.S.S. in the four-telescope configuration are given in Aharonian et al. (2006) and references therein.

The data used for the analysis of RX J0852.0−4622 were taken between 2004 and 2009; the bulk of the observations were performed between 2004 and 2006. The analysis of the data up to the end of 2005 has already been published (Aharonian et al. 2005, 2007). This work presents a re-analysis of the source motivated by a rough doubling of the data set. The exposure times (normalized to an offset of 0.7°) available for morphological and spectral analyses amount to 60 h and 39 h respectively. Thanks to the improved statistics more detailed studies of the morphology and the spectrum are possible. In addition, a spatially-resolved spectroscopy of the source can be performed.

The RX J0852.0−4622 data were analyzed with methods that are similar to the techniques discussed in Aharonian et al. (2006), however with two differences: gamma-hadron separation took advantage of a multi-variate approach (Ohm et al. 2009, instead of box cuts based on scaled Hillas parameters), and a forward-folding method with a likelihood technique similar to the one described in Piron et al. (2001) was used for spectrum derivation and flux measurements (instead of least-squares fitting). The results presented here were derived with the so-called HAP-HD analysis software and the corresponding instrument response tables. All results have been cross-checked with two independent software chains using an independent calibration of the data, yielding compatible results.

The extraction region or ON-source region (short: ON region) selected for the analysis is a circle centered at the nominal position of RX J0852.0−4622 (in right ascension and declination 8h52m, −46°22′12″, J2000) with a radius of 1.0°. This ON region is referred to as *whole SNR* in the following. To avoid any contamination from the nearby Vela X PWN (Abramowski et al. 2012) the region of the sky covering this source is excluded from the analysis, in particular in the estimation of cosmic-ray backgrounds from OFF-source regions (short: OFF regions).

Two different analysis configurations have been applied to the data when studying the morphological and spectral properties of RX J0852.0−4622, respectively:

– The *spatial* analysis was used to produce two-dimensional spatial skymaps in order to study the morphology of RX J0852.0−4622. This analysis is characterized by a loose

(less stringent) data selection criterion in which data taken under optimal atmospherical conditions, but varying instrumental conditions, are acceptable. Hard image cuts were used for data filtering in order to improve the angular resolution at the expense of statistics. Cosmic-ray backgrounds were estimated with the *ring background model* (Berge et al. 2007).

– The *spectral* analysis was used to produce flux measurements in order to study the photon spectrum of the entire SNR or of sub-regions (i.e. for spatially-resolved spectroscopy). This analysis is characterized by a stringent (conservative) data selection criterion aiming at reducing systematic errors by selecting only data taken under optimal atmospherical and instrumental conditions. Standard cuts were used for data filtering, and the *reflected region background model* (Berge et al. 2007) was applied for cosmic-ray background estimation.

Details of the data selection criteria and the cut configurations (hard, standard) can be found in Aharonian et al. (2006). The analysis of RX J0852.0−4622 is quite challenging since the regions used for signal extraction and for excluding nearby sources from the analysis are quite large with respect to the field of view of the instrument, as compared to other sources. A careful study of the systematic uncertainties showed a larger than usual variation of spectral parameters when comparing the results derived with different analysis chains in use within the H.E.S.S. Collaboration. The dispersion of the results yielded a systematic error on flux measurements of 25% and an error on spectral indices of 0.2 for spectral indices in the range from 1.5 to 2.2. The error of cut-off energies was found to be 20%. These uncertainties are slightly larger than the typical systematic errors given for H.E.S.S. in Aharonian et al. (2006); they do not represent the general trend of H.E.S.S. measurements.

3. Results

Table 1 summarizes the event statistics of all analyses applied to the data using the ON region detailed above to encompass the entire SNR, and of other smaller regions to study spectral details of the different parts of RX J0852.0−4622 in the spatially-resolved spectroscopy studies presented in Sect. 3.3. The specific parameters for all regions used are defined in the appendix in Table A.1.

3.1. Source Morphology

The spatial analysis of RX J0852.0−4622 (cf. first row of Table 1) is based on a data set with a total livetime of 93.6 h and results in a total significance is 39.1σ. The difference between the livetime of the analysis and the exposure time previously quoted is due to the fact that a large fraction of the available observations were targeting nearby sources, had large offsets and hence a small effective exposure time. The angular resolution attained in the morphological analysis is characterized by a PSF width (68% containment radius) of 0.08°. This angular resolution is larger than the 0.06° reported for the morphological analysis in Aharonian et al. (2007) since the default telescope multiplicity (≥ 2 telescopes per event) was respected in the analysis presented here. This favors γ-ray efficiency at the expense of a somewhat larger angular resolution. Figure 1 (left) shows the excess map corrected for the gradient of exposure across the field of view and smoothed with a Gaussian function with a width equal to the PSF width of 0.08°. The TeV emission matches the

region	analysis	$\langle\theta_{zen}\rangle$	$\langle\theta_{az}\rangle$	$\langle\theta_{off}\rangle$	t [h]	N_{ON}	N_{OFF}	α	excess	significance
whole SNR	spatial	29°	194°	1.4°	93.6	34025	16854	1.4	10332	39.1σ
whole SNR	spectral	32°	207°	1.2°	21.0	43363	36097	1.0	7266	25.8σ
NW rim	spectral	32°	204°	1.4°	28.8	17561	32212	0.4	4232	29.0σ
0	spectral	32°	206°	1.2°	31.3	24873	51436	0.4	3857	21.6σ
1	spectral	30°	201°	0.95°	18.4	5290	18586	0.2	949	12.5σ
2	spectral	31°	200°	1.0°	27.8	6912	27412	0.2	1058	12.1σ
3	spectral	32°	200°	0.92°	22.2	6639	21000	0.3	1342	15.7σ
4	spectral	32°	202°	0.91°	19.1	5315	12941	0.3	1062	13.5σ
5	spectral	31°	197°	1.1°	30.8	7163	27146	0.2	1469	16.9σ
6	spectral	30°	203°	0.93°	17.4	5189	10461	0.4	1261	16.1σ
A	spectral	31°	200°	1.2°	38.0	1151	14813	0.061	248	7.7σ
B	spectral	31°	200°	1.2°	38.0	8127	34927	0.19	1513	16.4σ
C	spectral	32°	202°	1.2°	35.6	27852	47530	0.49	4718	24.4σ
D	spectral	32°	201°	1.2°	38.8	1180	15587	0.057	298	9.3σ
B'	spectral	31°	200°	1.2°	38.0	6976	29997	0.19	1264	14.7σ
C'	spectral	32°	202°	1.2°	35.6	19594	33898	0.49	3144	19.3σ

Table 1. Statistics of the different analyses of the RX J0852.0−4622 data set. For each analysis, the table shows the name of the region analyzed, the applied analysis type, the mean zenith and azimuth angles of the observations ($\langle\theta_{zen}\rangle$ and $\langle\theta_{az}\rangle$ respectively), the mean offset angle $\langle\theta_{off}\rangle$, the livetime t, the number of events in the signal (ON) region N_{ON}, the number of events in the background (OFF) region N_{OFF}, the exposure normalization (ratio of ON to OFF exposures) α, the number of excess counts in the ON region and the significance of the signal in the ON region in number of Gaussian standard deviations σ.

shape of the SNR shell well, when comparing to measurements in radio and X-rays; the brightest region is a semicircular arc in the NW (the NW rim), and there are two other bright regions towards the South and South-East. With an extension of $\sim 2°$ in diameter, RX J0852.0−4622 is one of the largest known TeV sources in the sky.

The ON region (shown in Fig. 1, right) is in fact slightly too small since it barely encompasses the 5σ significance contour. It was chosen due to the large extension of the source; an even larger ON region would make the determination of OFF regions within the same field of view very difficult, thereby reducing the effective data set available, especially for the spectral studies (cf. Sect. 3.2). The number of γ-rays left outside the ON region is small ($\sim 5\%$) compared to the signal inside and its systematic uncertainty. In the following, the effect is therefore neglected. Nevertheless, in order to avoid background contamination, a larger region covering the whole RX J0852.0−4622 emission has been excluded for the determination of suitable OFF regions.

Projections of the skymap in Fig. 1 were calculated from the unsmoothed data, and the resulting photon counts were normalized to the covered solid angle. Inspection of the radial profile (i.e. a skymap projection along the radial coordinate; profile not shown here) confirms the earlier result that the emission comes from a thin shell and not from a sphere (Aharonian et al. 2007). The azimuthal profile (i.e. skymap projection along the azimuthal coordinate) calculated for an annulus with inner and outer radius of respectively 0.6° and 1.0° around the center of RX J0852.0−4622 is shown in Fig. 2. The azimuth angle is defined anti-clockwise from North. Two periods separated by a dashed gray line are shown; green and black dashed lines at 121° and 168° respectively, denote the position of PSR J0855−4644 and the center of the enhancement seen towards the South of the shell.

The azimuthal profile clearly shows that the emission is not homogeneous along the shell. In general, the NW rim (from 220° to 400°) is brighter than the south-eastern part of the shell, where a region of high emission is observed between the southern ($\sim$ 160°) and the south-eastern ($\sim$ 120°) enhancements. The emis-

sion in the South-East (cf. Fig. 2 (left)) is coincident with the position of the pulsar PSR J0855−4644. The emission roughly in the South is found to be coincident with the *Fermi*-LAT source 2FGL J0853.5−4711 (one of the three point-like sources in the 2FGL *Fermi*-LAT catalog[3] associated with RX J0852.0−4622 as indicated in Lande et al. (2012) and Nolan et al. (2012)) and very close to the radio source PMN J0852−4712 (see Wright et al. 1994). This morphology is also seen in radio and X-ray maps (Stupar et al. 2005) where most of the emission comes from the NW rim of the shell, with some local enhancements towards the South. In X-rays, an enhancement is also seen towards the direction of PSR J0855−4644.

### 3.2. Gamma-Ray Spectrum of the Whole SNR

The increased data set for RX J0852.0−4622 allows a deeper study of the emission spectrum of the entire SNR. After data quality selection, the available exposure only amounts to 21.0 h since a sizable fraction of the available observations is not usable for spectrum determination due to the large extent of the ON region and the exclusion region for Vela X. It is noted that many of the smaller ON regions used in the spatially-resolved spectroscopy analysis in Sect. 3.3 achieve a better data efficiency. The statistics and the properties of the ON region encompassing the whole SNR are shown in row 2 of Table 1. The spectrum was calculated in the energy range from 0.3 TeV to 30 TeV using the forward-folding technique assuming the three models listed in Table 2: a plain power law (PL), a curved power law (CPL) and a power law with exponential cut-off (ECPL). In the latter model, the parameter $\lambda = 1/E_{cut}$ is used in the fit because its error has a more Gaussian-like distribution than that of E_{cut}.

The best parameters found for all three models are presented in Table 3 (central section). A likelihood ratio test (based on Wilks' theorem (Wilks 1938)) is used to select the model that describes the data best. The null hypothesis is the PL model and the alternative hypothesis is either the CPL or the ECPL model.

---

[3] The subsequent 3FGL *Fermi*-LAT catalog (Acero et al. 2015) models RX J0852.0−4622 as an extended source (3FGL J0852.7−4631e) and does not list a counterpart.
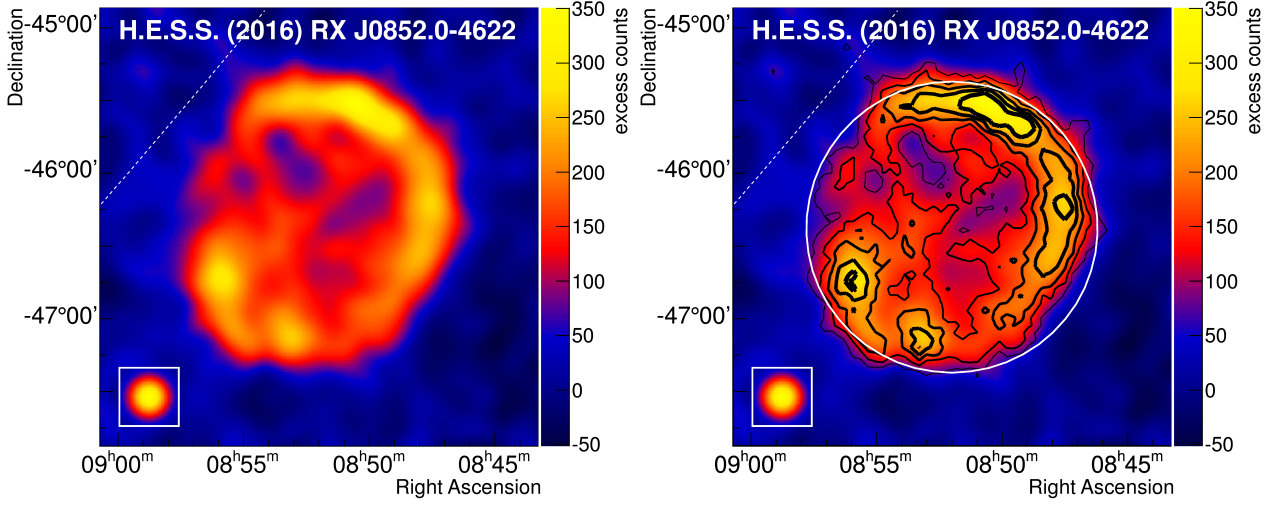
Fig. 1. Left: Exposure-corrected excess map for RX J0852.0−4622. The data have been binned in bins of 0.01° on each coordinate and smoothed with a Gaussian function of width 0.08°. The white dashed line shows the position of the Galactic plane; the inset shows the PSF of the analysis at the same scale for comparison. Right: Same as in the left panel, but additionally the boundary of the ON region is shown as a white circle and the significance contours at 3, 5, 7, 9 and 11σ are shown in black, with increasing line width for increasing significance.
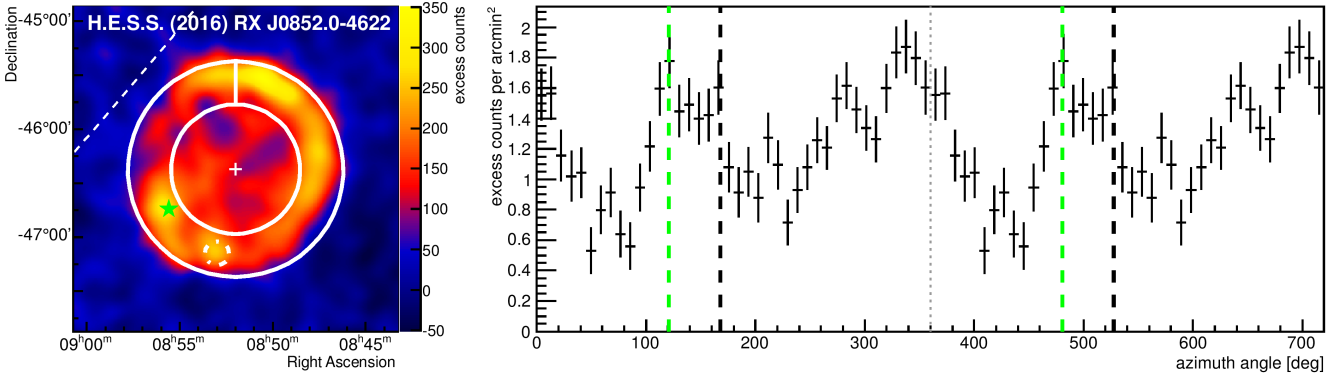
Fig. 2. Left: Smoothed and exposure-corrected excess map, like in Fig. 1. The white annulus denotes the region used for extraction of the azimuthal profile; the white vertical line denotes the origin of the azimuthal angle (North), which increases in the anti-clockwise direction. The green star marks the position of PSR J0855−4644. The white dotted-dashed line marks a point-like region around the position of the southern enhancement. Right: The azimuthal profile extracted from the annulus in the skymap on the left panel is shown. For better visibility, two periods separated by a dashed gray line are shown. The azimuthal position of PSR J0855−4644 and the center of the region around the southern enhancement are marked respectively by green and black vertical dashed lines.

model	formula	parameters
PL	$d\Phi/dE = \Phi_0(E/E_0)^{-\Gamma}$	Φ_0, Γ
CPL	$d\Phi/dE = \Phi_0(E/E_0)^{-\Gamma-\beta\log(E/E_0)}$	Φ_0, Γ, β
ECPL	$d\Phi/dE = \Phi_0(E/E_0)^{-\Gamma}\exp(-E/E_{cut})$	$\Phi_0, \Gamma, 1/E_{cut}$

Table 2. Spectrum models. For each model, the formula and the fit parameters are shown. The models are power law (PL), curved power law (CPL, also known as logarithmic parabola) and power law with exponential cut-off (ECPL).

Both alternative models are allowed to fall back into the PL during the fit, fulfilling the nested hypotheses requirement for the test.

The results of the likelihood ratio tests are shown in the right section of Table 3. The PL model is rejected at the 7.3σ level by the CPL model, and with 7.7σ by the ECPL model. This demonstrates that a curved spectrum is clearly preferred over a plain PL, implying that an intrinsic curvature exists in the spectrum of RX J0852.0−4622. Since the ECPL model shows the highest significance, it will be used in the following as the model describing the data best. More complex models (power law with sub or super exponential cut-off) have been tested as well but are not significantly better than any of the two curved models with 3 parameters.

The H.E.S.S. spectrum of RX J0852.0−4622 is shown in Fig. 3 together with the *Fermi*-LAT spectrum from Tanaka

model	Φ_0 [cm^{-2}s^{-1}TeV^{-1}]	Γ	β	E_{cut} [TeV]	$\log L$	NFP	significance
PL	$(27.4 \pm 0.9)\,10^{-12}$	2.30 ± 0.03	n/a	n/a	-51.717	2	n/a
CPL	$(28.8 \pm 1.1)\,10^{-12}$	1.89 ± 0.07	0.23 ± 0.04	n/a	-24.567	3	7.3σ
ECPL	$(32.2 \pm 1.5)\,10^{-12}$	1.81 ± 0.08	n/a	6.7 ± 1.2	-21.623	3	7.7σ

Table 3. Parameters of the spectral fits of the entire SNR and results of the likelihood ratio tests for each of the models from Table 2. The central section of the table lists the fit parameters. In the case of the power law with exponential cut-off, E_{cut} is shown instead of the fitted parameter $\lambda = 1/E_{cut}$. The quoted errors represent 1σ statistical uncertainties. In all cases the reference energy E_0 was chosen to be 1 TeV. The right section of the table shows the results of the likelihood ratio test in order to check for the existence of a curvature in the spectrum. For each fitted model the logarithm of the likelihood L, the number of free parameters NFP and the equivalent significance of the probability of the test in Gaussian standard deviations σ are shown. The test results apply to the comparison of a certain model with respect to the simpler (i.e. power-law) model.

parameter		H.E.S.S.	H.E.S.S. and *Fermi*-LAT
Φ_0	$[10^{-12}$ cm^{-2}s^{-1}TeV$^{-1}]$	$32.2 \pm 1.5_{stat} \pm 7.1_{syst}$	$31.6 \pm 1.4_{stat} \pm 7.6_{syst}$
Γ		$1.81 \pm 0.08_{stat} \pm 0.20_{syst}$	$1.79 \pm 0.02_{stat} \pm 0.10_{syst}$
E_{cut}	[TeV]	$6.7 \pm 1.2_{stat} \pm 1.2_{syst}$	$6.6 \pm 0.7_{stat} \pm 1.3_{syst}$
E_0	[TeV]	1	1
$E_{min} - E_{max}$	[TeV]	$0.3 - 30$	$0.001 - 30$
$F(> 1\,\text{TeV})$	$[10^{-12}$ cm^{-2}s$^{-1}]$	$23.4 \pm 0.7_{stat} \pm 4.9_{syst}$	
$F(0.3 - 30\,\text{TeV})$	$[10^{-12}$ cm^{-2}s$^{-1}]$	$84.1 \pm 4.3_{stat} \pm 21.7_{syst}$	

Table 4. Fit parameters for the H.E.S.S. spectrum (central column) and the joint H.E.S.S.-*Fermi*-LAT spectral fit (right column) of RX J0852.0−4622. The parameters refer to the power law with exponential cut-off model from Table 2. The parameter E_{cut} is shown instead of the fitted parameter $\lambda = 1/E_{cut}$. For the H.E.S.S. spectrum, the integral fluxes above 1 TeV ($F(> 1\,\text{TeV})$) and in the fitted range from 0.3 TeV to 30 TeV ($F(0.3 - 30\,\text{TeV})$), representing $\sim 113\%$ and $\sim 64\%$ of the flux of the Crab nebula in the same energy ranges respectively, are also shown. The quoted errors represent 1σ statistical and systematic uncertainties.
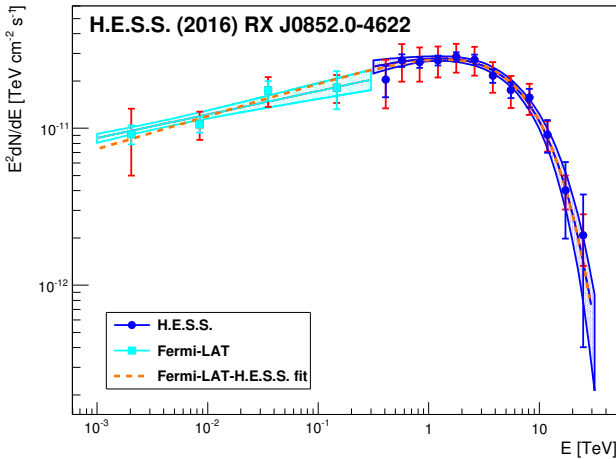
Fig. 3. H.E.S.S. and *Fermi*-LAT spectra for RX J0852.0−4622 with statistical and systematic errors. The *Fermi*-LAT measurement was taken from Tanaka et al. (2011). The figure shows the spectral points with 1σ statistical (light and dark blue lines for *Fermi*-LAT and H.E.S.S. respectively) and systematic (red lines in both cases) uncertainties together with the spectral fits and their 1σ statistical uncertainty (shaded bands). In addition, the simultaneous *Fermi*-LAT-H.E.S.S. fit function is also shown (orange dashed line).

et al. (2011). The H.E.S.S. spectral points and fit parameters are shown in Tables A.2 (in the appendix) and 4 (central column), respectively. The spectrum derived in this work represents a flux level that is 50% higher than derived in the previous publications (Aharonian et al. 2005, 2007). A careful study has revealed that the lower flux found in the earlier analyses was due to a lack of correction for the degradation of the telescope reflectivities when estimating γ-ray energies and fluxes. The revised flux makes RX J0852.0−4622 the brightest steady source

in the sky above 1 TeV with $F(E > 1\,\text{TeV}) = (23.4 \pm 0.7_{stat} \pm 4.9_{syst})\,10^{-12}$ cm^{-2}s^{-1} (a flux $\sim 13\%$ larger than the flux of the Crab nebula[4] in the same energy range) and results in a smooth connection of the GeV (*Fermi*-LAT) and TeV (H.E.S.S.) spectra (cf. Fig. 3). Indeed, the spectral break visible at the 5.4σ level (statistical; or 1.6σ systematic) between the GeV ($\Gamma = 1.85 \pm 0.06_{stat}{}^{+0.18_{syst}}_{-0.19_{syst}}$) and the TeV ($\Gamma = 2.24 \pm 0.04_{stat} \pm 0.15_{syst}$) spectra in Tanaka et al. (2011) is, with the current measurement from Table 4 (central column), only 0.4σ (statistical), i.e. non-existent.

Using both the *Fermi*-LAT and H.E.S.S. measurements, the ambiguity between the power law with exponential cut-off and curved power-law models can be solved. Indeed, a simultaneous fit of the *Fermi*-LAT and H.E.S.S. data points yields a χ^2 fit probability of 94% for a power law with exponential cut-off model, whereas the probability for the curved power law is 3.1×10^{-7}. The simultaneous *Fermi*-LAT-H.E.S.S. fit using the ECPL model is shown in Fig. 3 with an orange dashed line, and the fit parameters are shown in the rightmost column of Table 4. The systematic uncertainties of the parameters of the simultaneous fit have been determined from the variations observed when moving the *Fermi*-LAT points down (up) and the H.E.S.S. points up (down) by one standard deviation of their respective systematic uncertainties (this tests the systematic uncertainty of the spectral index and the cut-off energy) and by moving all data points down or up simultaneously (which tests the systematic uncertainty of the normalization).

A comparison of the parameter values of the simultaneous *Fermi*-LAT-H.E.S.S. fit and of the H.E.S.S. only spectrum (cf. Table 4) shows good agreement. The simultaneous fit shows smaller statistical uncertainties for all parameters (especially for the spectral index and cut-off energy), a smaller systematic uncertainty for the spectral index, a larger systematic uncertainty in

---

[4] Crab nebula fluxes in this work are calculated using the spectrum from Meyer et al. (2010).

the normalization and a similar systematic uncertainty in the cut-off energy. Thus, the simultaneous fit is able to better determine the spectral index and cut-off energy at the cost of a higher systematic uncertainty in the flux. The latter is due to the larger systematic error in the *Fermi*-LAT flux measurement ($\sim 30 - 35\%$).

3.3. Spatially-Resolved Spectroscopy

The increased data set on RX J0852.0−4622 and the size of the SNR allow for the first time a spatially-resolved spectroscopy, i.e. the derivation of spectra for subregions. For this purpose, different subregions of RX J0852.0−4622 have been defined following its γ-ray morphology and the location of the PWN around PSR J0855−4644 and the southern enhancement. As shown in Fig. 4 (top left), the SNR has been divided into a central part (region 0) and six regions (1–6) in the annulus covering the shell to test for spectral variations across the SNR. An additional region encompasses the 5σ significance contour around the bright NW rim (cf. Fig. 4, top center). Three circular regions around the position of PSR J0855−4644 (regions A, B and C in Fig. 4, top center) are used to estimate a possible PWN flux. Region A supposes a point-like source centered at the pulsar position. Region B encompasses the 7σ contour around the pulsar excluding the elongation to the South. Region C roughly encompasses the 5σ contour around the pulsar. Region D (cf. Fig. 4, top center) is adapted to a hypothetical point-like source for the southern enhancement observed in the skymap and the azimuthal profile (cf. Fig. 2). In addition, the regions B′ = B \ A (i.e. region B, excluding region A) and C′ = C \ B \ D (i.e. region C, excluding regions B and D) are used to search for a softening of the spectrum of the possible TeV PWN around PSR J0855−4644 (shaded areas in Fig. 4, top right). The specific parameters for all regions used are defined in the appendix in Table A.1.

Spectral analyses similar to those presented in Sect. 3.2 have been performed for each of the regions. The event statistics of all analyses are presented in Table 1. All analyzed regions show a clear signal with significances between 7.7σ and 29.0σ. The spectral parameters of a power law with exponential cut-off fitted to the data of each analyzed region in the energy range from 0.3 TeV to 30 TeV are shown in Table 5. The significance of the cut-off is listed in the rightmost column.

The central part of the SNR (region 0) and the shell towards the bright NW rim show a preference for a cut-off in the spectrum (test significance greater than 3σ); for the enhancement towards PSR J0855−4644 the significance of the cut-off is only 1.8σ for the point-like region (region A) but it grows with the size of the integration region (regions B and C). As for spectral variations across the RX J0852.0−4622 region, the shape of the spectrum of the NW rim is compatible with the spectrum of the whole SNR. It is also compatible with the spectra of the rest of the SNR at the 2σ level, when comparing to either regions C or 0, which largely cover the rest of the SNR emission. The spectra of the regions 0 to 6 do not show a clear deviation from the spectrum of the whole SNR ($\Gamma \sim 1.8$, $\lambda \sim 0.15\,\mathrm{TeV}^{-1}$), as shown by the overlapping error contours in Fig. 4 (bottom left); the variations of the spectral index Γ are smaller than $\pm 2\sigma$. Although region 2 seems to deviate from regions 1, 4 and 6, the effect is not significant, and indeed the weighted average of (Γ, λ) for regions 0 to 6 still yields a χ^2 probability of 4.8% (residual significance of 2.0σ), showing that all regions are compatible with a single (Γ, λ) pair. The spectra of the regions A and C also do not show a deviation from the spectra of either the whole SNR or the NW rim, as shown by the contour plot of Fig. 4 (bottom center). Region B shows some evidence of a harder spec-

trum with a larger cut-off energy compared to the NW rim (or the whole SNR); the significance for the cut-off in region B is not very high (only 2.7σ) and the deviation of index and cut-off energy is at the level of 3.5σ pre-trials (2.6σ post-trials[5]). Figure 4 (bottom right) shows that the spectral index of the possible TeV PWN remains basically constant when moving farther away from PSR J0855−4644 (region A to B′ to C′): no significant change in the spectral parameters is observed across the mentioned regions. This plot also shows that the spectrum of region D is compatible with the one of the NW rim and that the spectrum of region B′, although it comprises a smaller exposure than the one of region B, still shows marginal evidence for a difference with respect to the spectrum of the NW rim. The significance of the effect is 3.1σ pre-trials (2.1σ post-trials). Nevertheless, the weighted average of (Γ, λ) for regions A, B′, C′, D and the NW rim still yields a χ^2 probability of 6.6% (residual significance of 1.8σ).

4. Discussion

In the following, we will consider the implications of the new H.E.S.S. results on the understanding of the very-high-energy γ-ray emission from RX J0852.0−4622. The multiwavelength (MWL) data used in this section consist of:

- – Parkes radio data points from Duncan & Green (2000)
- – *ASCA* X-ray spectral fit from Aharonian et al. (2007)
- – *Fermi*-LAT GeV γ-ray points from Tanaka et al. (2011)
- – H.E.S.S. TeV γ-ray points from this work (cf. Fig. 3 and Table A.2 in the appendix).

The H.E.S.S. spectrum is not corrected for possible emission from a putative TeV PWN around PSR J0855−4644 (discussed in Sect. 4.3) since the expected flux contribution is smaller than the systematic error on the flux normalization.

4.1. Spectral Variations

The spatially-resolved spectroscopy analysis of RX J0852.0−4622 described in Sect. 3.3 does not show a significant variation of the spectral shape across the remnant. The regions which contain the PWN (cf. Fig. 4; discussed in Sect. 4.3) show some evidence for spectral variations but the effect is still below 3σ. This lack of apparent spectral variations suggests that the parent particle population is essentially the same across the remnant which in turn points to similar properties of the SNR shock and hence similar properties of the medium in which the shock was formed and is expanding. The invariability of the γ-ray spectral shape across the remnant allows a simple treatment of the MWL emission from RX J0852.0−4622, using one particle population for the entire SNR emission. This modeling obtains the average properties of the SNR and its surrounding medium.

4.2. Parent Particle Population

The increased exposure and careful study of the systematic effects strongly improved the quality of the spectrum of the whole SNR resulting in a smooth connection to the spectrum in the GeV band and in the determination of a clear cut-off (cf. Sect. 3.2). The smooth connection to the *Fermi*-LAT spectrum enables the study of the combined GeV-TeV spectrum,

---

[5] The post-trial significance takes into account that ~ 20 regions were tested in the search for spectral variations.
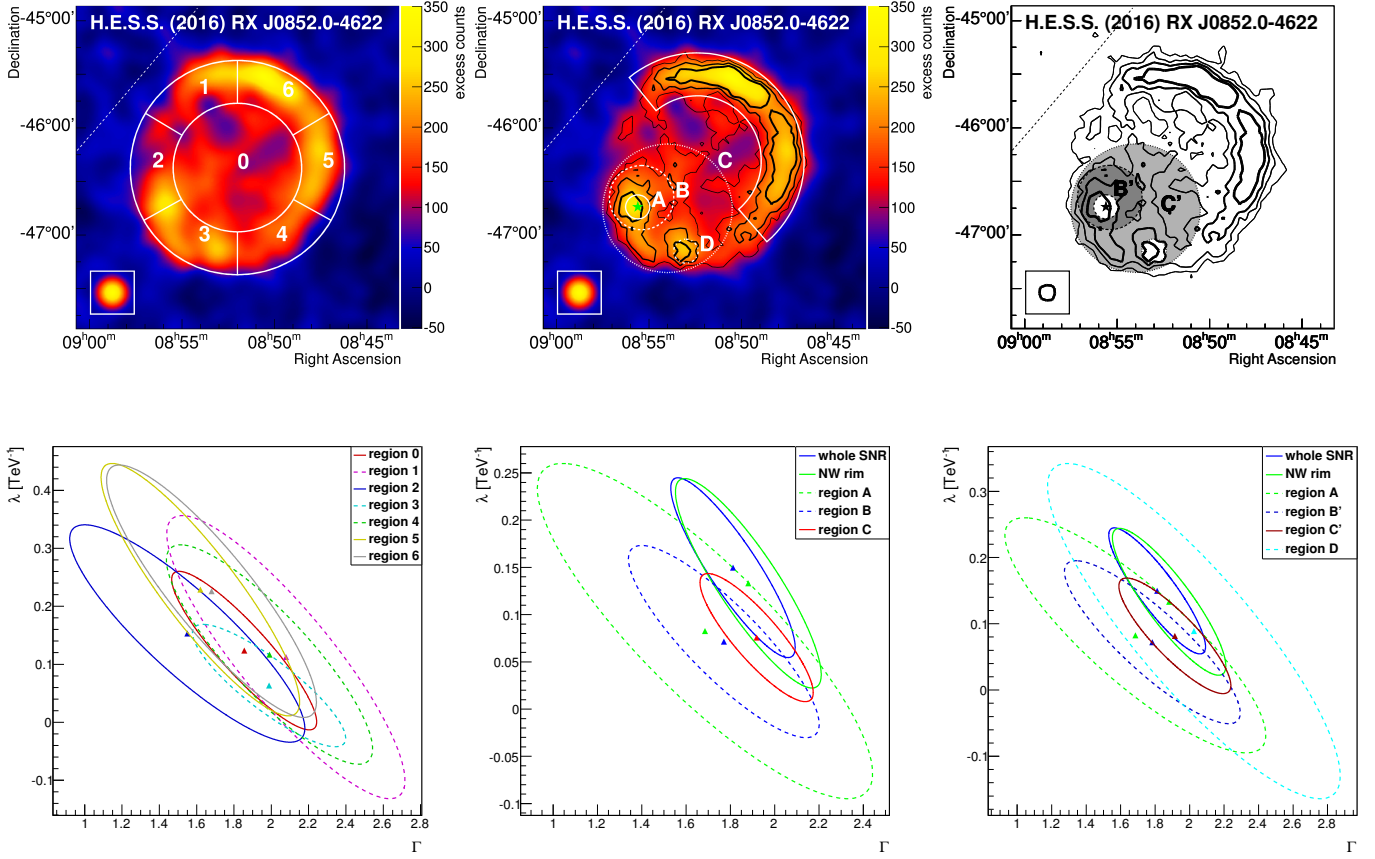
Fig. 4. The top figures display the skymaps (smoothed exposure-corrected excess map from Fig. 1 for the top left and center pads, significance contour map for the right pad) together with various regions used for the study of the spatially-resolved spectroscopy of the RX J0852.0−4622 region. Top left: with the regions 0 for the central part of the SNR and 1 − 6 for the shell in white. Center: with the regions A, B and C around PSR J0855−4644, region D around the southern enhancement in the azimuthal profile and the region used for the NW rim in white. The H.E.S.S. significance contours at 5, 7 and 9σ are shown in black, with increasing line width for increasing significance. The position of PSR J0855−4644 is marked by the green star. Top right: with the regions B′ (dark gray shaded area) and C′ (light gray shaded area) around PSR J0855−4644. The H.E.S.S. significance contours at 3, 5, 7 and 9σ are shown in black, with increasing line width for increasing significance. The position of PSR J0855−4644 is marked by the black star. The bottom figures represent the error contour plots of $\lambda = 1/E_{\text{cut}}$ versus Γ for the spectra of the regions in the excess maps assuming a power law with exponential cut-off model. For each region, the fitted value is marked with a triangle, while the ellipse marks the contour of the 3σ confidence level statistical uncertainty. Dashed lines are used for the regions where the cut-off significance is below 3σ. Bottom left: for the spectra of the regions 0 to 6. Bottom center: for the spectra of the regions A, B, C. In addition, the contours of the analysis of the whole SNR and the NW rim are shown. Since the spectra of regions A - C are correlated because the regions overlap, the corresponding contours are not meant to be compared to each other, but to the contours of the NW rim. Bottom right: for the spectra of the regions A, B′, C′, D. In addition, the contours of the analysis of the whole SNR and the NW rim are shown.

which in turn provides an opportunity to directly extract from the observational data the present-time parent particle population responsible for the γ-ray emission in leptonic and hadronic scenarios. The advantage of this approach is that the spectral shape of the present-time parent particle population can be obtained without assumptions made on the SNR evolution, its hydrodynamics, properties of the local magnetic field and energy losses which accelerated particles undergo. In this procedure we fit the *Fermi*-LAT and H.E.S.S. data points and their respective statistical errors (cf. Fig. 5) with the emission from parent electron or proton populations following a power law with an exponential cut-off

$$N_{\text{p,e}}(E) = \frac{N_{0,\text{p,e}}}{4\pi d^2} \left(\frac{E}{1\,\text{TeV}} \right)^{-p_{\text{p,e}}} \exp\left(-\frac{E}{E_{\text{cut, p,e}}} \right), \tag{1}$$

where $N_{0,\text{p,e}}$ is the normalization at 1 TeV, $p_{\text{p,e}}$ is the spectral index, $E_{\text{cut, p,e}}$ is the cut-off energy and d is the distance to the

SNR. The subscripts p (for protons) and e (for electrons) denote respectively the hadronic and leptonic scenarios. In order to evaluate the systematic uncertainty of our results we also fit the model when systematically shifting the *Fermi*-LAT and H.E.S.S. points in an analogous way as for the simultaneous *Fermi*-LAT-H.E.S.S. spectral fit in Sect. 3.2. The distance of 750 pc is adopted in these calculations. Uncertainties on the distance estimate impact only flux normalization and, hence, the estimate of the total energy in particles, but do not influence the spectral shape, i.e. the spectral index and the cut-off energy. The spectral index is determined by the smooth connection of the *Fermi*-LAT and H.E.S.S. spectra, while the cut-off energy of the accelerated particles is constrained by the cut-off in the H.E.S.S. γ-ray spectrum. The derivation of the present-time parent particle population is very important for further modeling of the source. Hadronic and leptonic scenarios can be tested based on

region	Φ_0 [10^{-12} cm^{-2}s^{-1}TeV^{-1}]	Γ	E_{cut} [TeV]	$F(> 1\,\text{TeV})$ [10^{-12} cm^{-2}s^{-1}]	$F(0.3 - 30\,\text{TeV})$ [10^{-12} cm^{-2}s^{-1}]	sign
whole SNR	$32.2 \pm 1.5(\pm 7.1)$	$1.81 \pm 0.08(\pm 0.20)$	$6.7 \pm 1.2(\pm 1.2)$	$23.4 \pm 0.7(\pm 4.9)$	$84.1 \pm 4.3(\pm 21.7)$	7.7σ
NW rim	$12.4 \pm 0.7(\pm 3.1)$	$1.88 \pm 0.10(\pm 0.20)$	$7.5 \pm 1.8(\pm 1.5)$	$8.9 \pm 0.4(\pm 2.2)$	$33.7 \pm 2.0(\pm 8.4)$	5.6σ
0	$8.9 \pm 0.6(\pm 2.2)$	$1.85 \pm 0.11(\pm 0.20)$	$8.1 \pm 2.6(\pm 1.6)$	$6.7 \pm 0.3(\pm 1.7)$	$24.1 \pm 1.6(\pm 6.0)$	4.5σ
1	$3.5 \pm 0.4(\pm 0.9)$	$2.08 \pm 0.19(\pm 0.20)$	$8.9 \pm 5.6(\pm 1.8)$	$2.34 \pm 0.20(\pm 0.59)$	$10.5 \pm 1.1(\pm 2.6)$	2.1σ
2	$2.4 \pm 0.3(\pm 0.6)$	$1.55 \pm 0.18(\pm 0.20)$	$6.5 \pm 2.3(\pm 1.3)$	$2.12 \pm 0.16(\pm 0.53)$	$5.9 \pm 0.7(\pm 1.5)$	3.9σ
3	$4.0 \pm 0.3(\pm 1.0)$	$1.99 \pm 0.12(\pm 0.20)$	$15.8 \pm 7.7(\pm 3.2)$	$3.19 \pm 0.19(\pm 0.80)$	$12.1 \pm 1.0(\pm 3.0)$	2.3σ
4	$3.8 \pm 0.4(\pm 1.0)$	$1.99 \pm 0.16(\pm 0.20)$	$8.6 \pm 4.0(\pm 1.7)$	$2.64 \pm 0.20(\pm 0.66)$	$10.9 \pm 1.1(\pm 2.7)$	2.7σ
5	$4.4 \pm 0.4(\pm 1.1)$	$1.62 \pm 0.15(\pm 0.20)$	$4.4 \pm 1.2(\pm 0.9)$	$2.99 \pm 0.17(\pm 0.75)$	$9.9 \pm 0.8(\pm 2.5)$	5.5σ
6	$5.2 \pm 0.5(\pm 1.3)$	$1.68 \pm 0.16(\pm 0.20)$	$4.4 \pm 1.2(\pm 0.9)$	$3.43 \pm 0.22(\pm 0.86)$	$12.0 \pm 1.1(\pm 3.0)$	4.9σ
A	$0.64 \pm 0.10(\pm 0.16)$	$1.69 \pm 0.22(\pm 0.20)$	$12.1 \pm 7.6(\pm 2.4)$	$0.62 \pm 0.07(\pm 0.15)$	$1.8 \pm 0.3(\pm 0.4)$	1.8σ
B	$2.34 \pm 0.19(\pm 0.59)$	$1.77 \pm 0.13(\pm 0.20)$	$14.0 \pm 5.8(\pm 2.8)$	$2.18 \pm 0.14(\pm 0.55)$	$6.6 \pm 0.7(\pm 1.7)$	2.7σ
C	$10.0 \pm 0.5(\pm 2.5)$	$1.92 \pm 0.07(\pm 0.20)$	$13.2 \pm 3.4(\pm 2.6)$	$8.2 \pm 0.3(\pm 2.1)$	$29.5 \pm 1.6(\pm 7.4)$	4.5σ
D	$0.81 \pm 0.12(\pm 0.20)$	$2.02 \pm 0.25(\pm 0.20)$	$11.2 \pm 9.3(\pm 2.2)$	$0.59 \pm 0.07(\pm 0.15)$	$2.4 \pm 0.4(\pm 0.6)$	1.4σ
B′	$1.88 \pm 0.18(\pm 0.47)$	$1.78 \pm 0.15(\pm 0.20)$	$13.9 \pm 6.9(\pm 2.8)$	$1.73 \pm 0.13(\pm 0.43)$	$5.4 \pm 0.6(\pm 1.3)$	2.3σ
C′	$6.7 \pm 0.4(\pm 1.7)$	$1.91 \pm 0.09(\pm 0.20)$	$12.2 \pm 3.8(\pm 2.4)$	$5.4 \pm 0.3(\pm 1.4)$	$19.6 \pm 1.4(\pm 4.9)$	3.8σ

Table 5. Spectral parameters for the spatially-resolved spectroscopy of RX J0852.0−4622 assuming a power-law with exponential cut-off model (ECPL in Table 2). All parameter sets were derived for spectra in the energy range from 0.3 TeV to 30 TeV and assuming a reference energy for the fit E_0 of 1 TeV. $F(> 1\,\text{TeV})$ and $F(0.3 - 30\,\text{TeV})$ represent the integral fluxes above 1 TeV and in the fitted range from 0.3 TeV to 30 TeV, respectively. The last column lists the equivalent significance in Gaussian standard deviations σ of the preference of a power-law with exponential cut-off model with respect to a simple power-law one, according to the likelihood ratio test. The quoted errors represent 1σ statistical (systematic in parentheses) uncertainties.
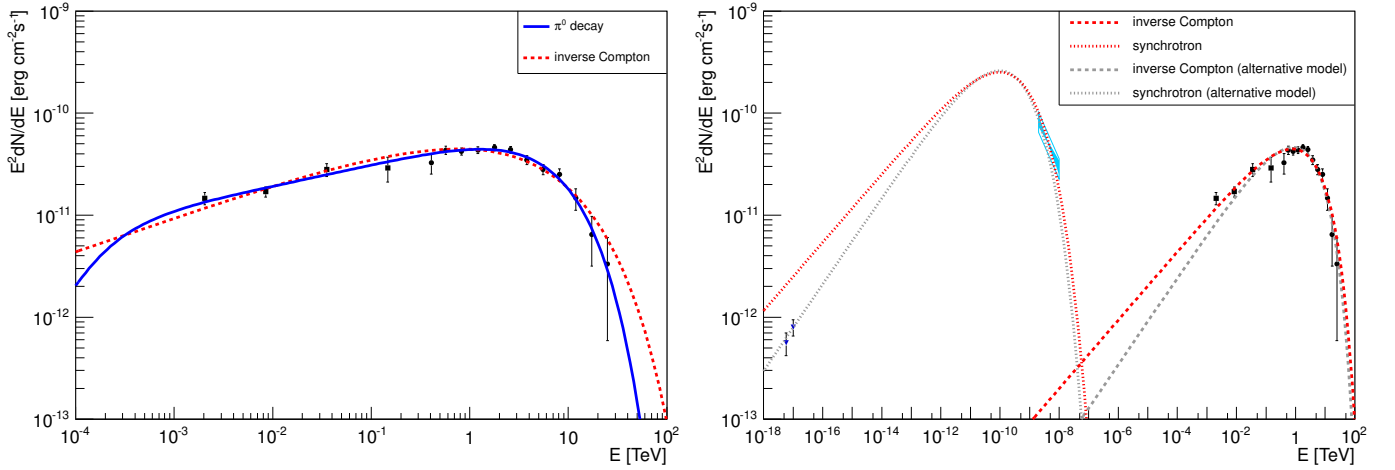
Fig. 5. Left: spectral energy distribution of SNR RX J0852.0−4622 in the GeV-TeV band. Filled squares reflect the emission detected by *Fermi*-LAT, while filled circles show the H.E.S.S. data. Error bars reflect statistical errors. Lines represent fits of the leptonic (dashed red) and hadronic (solid blue) γ-ray emission models to the data. Right: broadband spectral energy distribution of SNR RX J0852.0−4622 in the leptonic scenario. The MWL data are indicated as follows: radio - filled blue triangles, X-ray - cyan bowties, GeV γ-rays - filled squares, TeV γ-rays - filled circles. The error bars of the *Fermi*-LAT and H.E.S.S. data points reflect statistical errors only. The filled blue bowtie represents the 90% confidence level statistical uncertainty band on the X-ray data, the open bowtie represents systematic uncertainties. Red lines represent the emission from the electron population as obtained from the fit of the GeV-TeV data (cf. left Fig.) and gray lines represent the emission from a modified electron population where all parameters were decreased by 0.6σ of the quadratically added statistical and systematic uncertainties. Dashed lines correspond to the IC emission and dotted lines correspond to synchrotron radiation.

the attainability of the present-time particle population considering the physical properties of the SNR and its ambient medium.

4.2.1. Leptonic scenario

In the leptonic scenario, we assume that the GeV-TeV γ-ray emission from RX J0852.0−4622 is dominated by the IC emission from relativistic electrons scattered on ambient radiation fields. Besides the cosmic microwave background (CMB), local infrared (IR) and optical radiation fields might also contribute to the IC emission. However, it is often very difficult to estimate the spectrum of the local radiation fields due to the poor

knowledge of the environment. According to the interstellar radiation field (ISRF) model by Porter et al. (2006) the contribution of IR and optical radiation fields should be negligible due to the large distance between SNR RX J0852.0−4622 and the Galactic center (∼ 9 kpc). Stars detected in the field of view of RX J0852.0−4622 are not powerful enough to provide a strong radiation field and moreover, the high uncertainty on the determination of the distance to these stars makes it difficult to judge whether they are located in the proximity of the remnant or not (Iyudin et al. 2010). Therefore, we decided to adopt CMB as the only radiation field responsible for the IC scattering of relativistic electrons. The γ-ray emission is calculated according to Blumenthal & Gould (1970). The leptonic model (red dashed

scenario	parameter		value
hadronic	$\frac{N_{0,p}}{4\pi d^2}\,[n]^{-1}$	$[10^4\,\mathrm{TeV}^{-1}\mathrm{cm}^{-2}]$	$7.8 \pm 0.3(\pm 2.0)$
	p_p		$1.83 \pm 0.02(\pm 0.11)$
	$E_{\mathrm{cut},p}$	$[\mathrm{TeV}]$	$55 \pm 6(\pm 13)$
	$W_p\,[n]^{-1}$	$[10^{49}\mathrm{erg}]$	$7.1 \pm 0.3(\pm 1.9)$
leptonic	$\frac{N_{0,e}}{4\pi d^2}$	$[10^2\,\mathrm{TeV}^{-1}\mathrm{cm}^{-2}]$	$7.8 \pm 0.6(\pm 3.1)$
	p_e		$2.33 \pm 0.03(\pm 0.33)$
	$E_{\mathrm{cut},e}$	$[\mathrm{TeV}]$	$27 \pm 1(\pm 12)$
	W_e	$[10^{47}\mathrm{erg}]$	$4.1 \pm 0.3(\pm 1.7)$

Table 6. Best parameter sets of the fit of the parent particle distribution of Eq. (1) in the hadronic (subscript p for protons) and leptonic (subscript e for electrons) scenarios using solely the γ-ray data. $N_{0,p,e}$ represents the differential particle number at 1 TeV, $p_{p,e}$ the spectral index, $E_{\mathrm{cut},p,e}$ the cut-off energy, d the distance to the SNR, n the density of the ambient medium (in cm^{-3}), $W_{p,e}$ the total energy in accelerated particles above 100 GeV for electrons in the leptonic model and above 1 GeV for protons in the hadronic model. The quoted errors represent 1σ statistical (systematic in parentheses) uncertainties.

line in Fig. 5 left) provides a good fit to the *Fermi*-LAT-H.E.S.S. data with $\chi^2/\mathrm{NDF} = 13.8/13$ (χ^2 probability 0.39). The best-fit parameters are shown in Table 6. The integration of the electron spectrum above 100 GeV yields a total energy in electrons $W_e = (4.1 \pm 0.3_{\mathrm{stat}} \pm 1.7_{\mathrm{syst}})\,10^{47}$ erg.

A magnetic field strength of $7\,\mu$G is needed to explain the observed X-ray flux by synchrotron emission from the obtained electron population (red dotted line in Fig. 5 right). The modeled synchrotron spectrum does not reproduce well the slope of the observed X-ray spectrum within its statistical uncertainty, but both agree within the systematics of the X-ray spectrum. The same synchrotron emission overpredicts the radio flux. However, a decrease of the values of all parameters by 0.6σ of the quadratically added statistical and systematic uncertainties allows us to accommodate the radio data within our leptonic model (gray dotted line in Fig. 5 right).

For such a low magnetic field, synchrotron cooling effects are negligible and do not have a significant impact on the energy spectrum of the electron population. Indeed, following Blumenthal & Gould (1970) and adopting an SNR age of 3000 yr, the break energy above which the synchrotron losses become important is

$$E_b \simeq 90 \left(\frac{t_{\mathrm{age}}}{3000\,\mathrm{yr}}\right)^{-1} \left(\frac{B}{7\,\mu\mathrm{G}}\right)^{-2} \mathrm{TeV},$$

which is considerably higher than the obtained electron cut-off energy. This result suggests that the electron spectrum of RX J0852.0−4622 may be limited by the age of the SNR (see e.g. Reynolds 1998) rather than by radiative losses, or that the SNR is considerably younger than 3000 yr. A typical acceleration time for the electrons to reach the energy of 27 TeV in the magnetic field of $7\,\mu$G for the shock compression ratio of 4 is (Parizot et al. 2006)

$$t_{\mathrm{acc}} = 1.3\eta \left(\frac{E_{\mathrm{cut},e}}{27\,\mathrm{TeV}}\right) \left(\frac{B}{7\,\mu\mathrm{G}}\right)^{-1} \left(\frac{V_s}{3000\,\mathrm{km/s}}\right)^{-2} \mathrm{kyr},$$

where V_s is the shock velocity and η expresses the deviation of the diffusion coefficient from Bohm diffusion. However, it should be noted here that the magnetic field could have been higher in the past, in which case synchrotron losses can still play a major role.

The obtained value of the magnetic field strength is in very good agreement with the values obtained in other leptonic models available in the literature (see e.g. Lee et al. 2013). It represents the average magnetic field across the remnant and does not exclude the existence of regions with higher or lower magnetic fields; it is, however, in conflict with the significantly amplified magnetic fields derived for the filamentary structures in the NW rim under the hypothesis that the filament width is limited by synchrotron cooling.

4.2.2. Hadronic scenario

In the hadronic scenario, we assume that the observed GeV-TeV γ-ray emission is dominated by γ-rays produced in hadronic interactions. The γ-ray emission is calculated according to Kelner et al. (2006). The hadronic model (blue, solid line in Fig. 5) fits the *Fermi*-LAT-H.E.S.S. data very well with $\chi^2/\mathrm{NDF} = 6.0/13$ (χ^2 probability 0.95). The best-fit parameters are shown in Table 6. The integration of the proton spectrum above 1 GeV yields a total energy in protons $W_p = (7.1 \pm 0.3_{\mathrm{stat}} \pm 1.9_{\mathrm{syst}})\,10^{49} \left[\frac{n}{1\,\mathrm{cm}^{-3}}\right]^{-1}$ erg, where n is the density of the ambient medium.

The lack of thermal X-rays suggests a density of the ambient medium significantly lower than $1\,\mathrm{cm}^{-3}$ (Slane et al. 2001). This in turn, would require an unrealistically high estimate of the energy transferred to protons, comparable to or even higher than the total energy of $\sim 10^{51}$ erg provided by the SN explosion. This problem, however, can be solved if the SNR is expanding in a very inhomogeneous clumpy environment as shown for RX J1713.7−3946 (Inoue et al. 2012; Gabici & Aharonian 2014). Modeling such a scenario is beyond the scope of this paper.

The proton spectral index obtained in the GeV-TeV fit ($1.83 \pm 0.02_{\mathrm{stat}} \pm 0.11_{\mathrm{syst}}$) is slightly harder than the value of 2.0 expected in the diffusive shock acceleration for strong shocks with compression ratio of 4. However, from most of the SNRs detected at gamma-ray energies, an even steeper spectrum of protons is inferred (see e.g. Caprioli 2011). The hard proton spectrum (index 1.8) implied by the fit of the GeV-TeV emission from RX J0852.0−4622 requires further theoretical investigation.

4.3. Pulsar Wind Nebula Around PSR J0855−4644

The pulsar population study by H.E.S.S. Collaboration et al. (2016b) shows that wind nebulae of energetic pulsars are very likely to be detectable in γ-rays at TeV energies. Since PSR J0855−4644 falls into this category, it is quite likely that some of the emission attributed to RX J0852.0−4622 could come from a possible TeV PWN associated to PSR J0855−4644. The H.E.S.S. point-spread function does not allow for a separation of the emissions due to the PWN and the SNR. Nevertheless, the flux measurements in the regions A - C from Table 5 can be interpreted as flux upper limits on a possible TeV PWN associated to PSR J0855−4644, for different size assumptions of the PWN. Different sizes of the putative TeV PWN were assumed due to the lack of knowledge of its potential size at TeV energies. For pulsars older than ~ 10 kyr the size of the TeV PWN can be up to $100 - 1000$ times larger than the size of the X-ray PWN (Kargaltsev & Pavlov 2010) due to particle propagation up to large distances from the pulsar through diffusion/advection processes and/or proper motion of the pulsar itself.

Region B is the only region with spectral parameters deviating more than 3σ (3.5σ pre-trials, 2.6σ post-trials) from the

spectrum of the NW rim, which might be suggestive of a PWN contribution to the flux in this region. The insignificant deviation of the spectra of the regions A and C from the rest of the remnant can be naturally explained by the sizes of these two regions. On the one hand, the small size of region A results in low statistics and hence high uncertainties in the spectral parameters. On the other hand, with its much larger size, region C comprises a significant part of the SNR interior and other parts of the shell, leading to the domination of the emission from the SNR over the emission from the PWN. Therefore, the deviation of the spectrum of region B from the spectrum of the rest of the SNR not only points to the contribution from the PWN but also constrains the size of the putative PWN. Moreover, the γ-ray spectrum of region B deviates from the spectrum of the rest of the SNR in the same way as the X-ray spectrum of the PWN differs from the spectrum of the SNR, which further supports the hypothesis of significant contribution of the PWN emission to the γ-ray flux in region B. The X-ray spectrum of the PWN is significantly harder than the spectrum of the SNR (Acero et al. 2013), which agrees well with an increase of the cut-off energy of the γ-ray spectrum of region B with respect to the rest of the remnant.

The γ-ray emission from the PWN might provide a substantial contribution to the overall flux from RX J0852.0−4622. Adopting the size of region B as a potential size of the putative TeV PWN, this contribution can be as large as ∼ 8% of the total γ-ray flux from the SNR, considering the flux level measured for region B. However, it should be noted that the γ-ray emission from the remnant also contributes to the flux from region B and hence only a fraction of the γ-ray emission detected in that region is due to the PWN. The azimuthal profile (cf. Fig. 2) exhibits approximately double the flux at the position coincident with the X-ray PWN compared to the regions around it. Therefore, a more plausible prediction for the fraction of the γ-ray emission from the PWN in the overall flux from RX J0852.0−4622 is about 4%. This was not taken into account in the modeling of the SNR presented above, assuming that all the detected γ-ray flux is coming from RX J0852.0−4622. However, if the contribution of the PWN is indeed only around 4% of the overall flux, it would be well covered by the systematic errors estimated for the GeV and TeV data. Even an 8% contribution would be covered by the 25% systematic error assigned to the overall flux.

5. Conclusions

The analysis of an enlarged H.E.S.S. data set, using approximately double the observation time compared to previous publications, comes to the following conclusions:

1. A revised flux measurement makes RX J0852.0−4622 the brightest steady source in the sky above 1 TeV with $F(> 1\,\text{TeV}) = (23.4 \pm 0.7_{\text{stat}} \pm 4.9_{\text{syst}})\,10^{-12}\,\text{cm}^{-2}\text{s}^{-1}$, a flux ∼ 13% larger than the flux of the Crab nebula in the same energy range.
2. The energy spectrum of RX J0852.0−4622 is clearly curved and has an exponential cut-off at $E_{\text{cut}} = (6.7 \pm 1.2_{\text{stat}} \pm 1.2_{\text{syst}})\,\text{TeV}$. The determination of the cut-off helps to better characterize the parent particle population.
3. The new TeV spectrum connects well with the *Fermi*-LAT measurement at GeV energies without the need for a spectral break as in previous publications. This smooth connection of the GeV and TeV spectra together with the well-defined cut-off allows us to directly determine the characteristics of the parent particle population in both leptonic and hadronic scenarios.

4. The study of the spatially-resolved spectroscopy reveals no clear spectral variation across the SNR, suggesting that the parent particle population can be assumed to be the same throughout the remnant, which in turn indicates that the conditions for particle acceleration, i.e. properties of the SNR shock and ambient medium, are similar everywhere.
5. The enhancement detected towards PSR J0855−4644 suggests that some of the emission might come from a possible TeV PWN associated to the PSR. The contribution is estimated to be less than 8%.

Deeper H.E.S.S. observations of RX J0852.0−4622 thus provide a significant improvement of statistics revealing the existence of a cut-off in the TeV spectrum, which in turn considerably improves the characterization of the parent particle population and allows, for the first time, the estimation of the uncertainties of its parameters. Both leptonic and hadronic models remain plausible as they both provide a good fit of the data. Larger statistics at high energies (i.e. above 10 TeV) providing a better characterization of the spectral cut-off could give more insight into the nature of the parent particle population for this object. Such data could be obtained with even deeper H.E.S.S. observations and ultimately from the future CTA (Actis et al. 2011) observatory. In addition, larger statistics and better angular resolution should help in the search for clear spectral variations across the RX J0852.0−4622 region, such as a softening of the spectrum, when moving away from PSR J0855−4644. Moreover, smaller errors on the spectral parameters would also allow the establishment of spectral differences between region B and the NW rim. All this would help in separating the contributions from the PWN and the SNR.

References

Abramowski, A., Acero, F., Aharonian, F., et al. 2012, A&A, 548, A38
Acero, F., Ackermann, M., Ajello, M., et al. 2015, ApJS, 218, 23
Acero, F., Gallant, Y., Ballet, J., Renaud, M., & Terrier, R. 2013, A&A, 551, A7
Actis, M., Agnetta, G., Aharonian, F., et al. 2011, Experimental Astronomy, 32, 193
Aharonian, F., Akhperjanian, A. G., Bazer-Bachi, A. R., et al. 2006, A&A, 457, 899
Aharonian, F., Akhperjanian, A. G., Bazer-Bachi, A. R., et al. 2005, A&A, 437, L7
Aharonian, F., Akhperjanian, A. G., Bazer-Bachi, A. R., et al. 2007, ApJ, 661, 236
Allen, G. E., Chow, K., DeLaney, T., et al. 2015, ApJ, 798, 82
Aschenbach, B. 1998, Nature, 396, 141
Aschenbach, B., Iyudin, A. F., & Schönfelder, V. 1999, A&A, 350, 997
Bamba, A., Yamazaki, R., & Hiraga, J. S. 2005, ApJ, 632, 294
Berezhko, E. G., Pühlhofer, G., & Völk, H. J. 2009, A&A, 505, 641
Berge, D., Funk, S., & Hinton, J. 2007, A&A, 466, 1219
Blumenthal, G. R. & Gould, R. J. 1970, Reviews of Modern Physics, 42, 237
Caprioli, D. 2011, J. Cosmology Astropart. Phys., 5, 026

Duncan, A. R. & Green, D. A. 2000, A&A, 364, 732

Gabici, S. & Aharonian, F. A. 2014, MNRAS, 445, L70

Green, D. A. 2009, Bulletin of the Astronomical Society of India, 37, 45

H.E.S.S. Collaboration, Abdalla, H., Abramowski, A., et al. 2016a, H.E.S.S. observations of RX J1713.7−3946 with improved angular and spectral resolution; evidence for gamma-ray emission extending beyond the X-ray emitting shell, A&A forthcoming

H.E.S.S. Collaboration, Abdalla, H., Abramowski, A., et al. 2016b, The Population of TeV Pulsar Wind Nebulae in the H.E.S.S. Galactic Plane Survey, A&A forthcoming

Inoue, T., Yamazaki, R., Inutsuka, S., & Fukui, Y. 2012, ApJ, 744, 71

Iyudin, A. F., Pakhomov, Y. V., Chugai, N. N., et al. 2010, A&A, 519, A86

Kargaltsev, O. & Pavlov, G. G. 2010, X-ray Astronomy 2009; Present Status, Multi-Wavelength Approach and Future Perspectives, 1248, 25

Katagiri, H., Enomoto, R., Ksenofontov, L. T., et al. 2005, ApJ, 619, L163

Katsuda, S., Tsunemi, H., & Mori, K. 2008, ApJ, 678, L35

Kelner, S. R., Aharonian, F. A., & Bugayov, V. V. 2006, Phys. Rev. D, 74, 034018

Kishishita, T., Hiraga, J., & Uchiyama, Y. 2013, A&A, 551, A132

Lande, J., Ackermann, M., Allafort, A., et al. 2012, ApJ, 756, 5

Lee, S.-H., Slane, P. O., Ellison, D. C., Nagataki, S., & Patnaude, D. J. 2013, ApJ, 767, 20

Meyer, M., Horns, D., & Zechlin, H.-S. 2010, A&A, 523, A2

Nolan, P. L., Abdo, A. A., Ackermann, M., et al. 2012, ApJS, 199, 31

Obergaulinger, M., Iyudin, A. F., Müller, E., & Smoot, G. F. 2014, MNRAS, 437, 976

Ohm, S., van Eldik, C., & Egberts, K. 2009, Astroparticle Physics, 31, 383

Parizot, E., Marcowith, A., Ballet, J., & Gallant, Y. A. 2006, A&A, 453, 387

Piron, F., Djannati-Atai, A., Punch, M., et al. 2001, A&A, 374, 895

Pohl, M., Yan, H., & Lazarian, A. 2005, ApJ, 626, L101

Porter, T. A., Moskalenko, I. V., & Strong, A. W. 2006, ApJ, 648, L29

Rettig, R. & Pohl, M. 2012, A&A, 545, A47

Reynolds, S. P. 1998, ApJ, 493, 375

Reynoso, E. M., Dubner, G., Giacani, E., Johnston, S., & Green, A. J. 2006, A&A, 449, 243

Slane, P., Hughes, J. P., Edgar, R. J., et al. 2001, ApJ, 548, 814

Stupar, M., Filipović, M. D., Jones, P. A., & Parker, Q. A. 2005, Advances in Space Research, 35, 1047

Takeda, S., Bamba, A., Terada, Y., et al. 2016, PASJ, 68, S10

Tanaka, T., Allafort, A., Ballet, J., et al. 2011, ApJ, 740, L51

Telezhinsky, I. 2009, Astroparticle Physics, 31, 431

Wilks, S. S. 1938, The Annals of Mathematical Statistics, 9, 60

Wright, A. E., Griffith, M. R., Burke, B. F., & Ekers, R. D. 1994, ApJS, 91, 111

[1] Centre for Space Research, North-West University, Potchefstroom 2520, South Africa

[2] Universität Hamburg, Institut für Experimentalphysik, Luruper Chaussee 149, D 22761 Hamburg, Germany

[3] Max-Planck-Institut für Kernphysik, P.O. Box 103980, D 69029 Heidelberg, Germany

[4] Dublin Institute for Advanced Studies, 31 Fitzwilliam Place, Dublin 2, Ireland

[5] National Academy of Sciences of the Republic of Armenia, Marshall Baghramian Avenue, 24, 0019 Yerevan, Republic of Armenia

[6] Yerevan Physics Institute, 2 Alikhanian Brothers St., 375036 Yerevan, Armenia

[7] Institut für Physik, Humboldt-Universität zu Berlin, Newtonstr. 15, D 12489 Berlin, Germany

[8] University of Namibia, Department of Physics, Private Bag 13301, Windhoek, Namibia

[9] GRAPPA, Anton Pannekoek Institute for Astronomy, University of Amsterdam, Science Park 904, 1098 XH Amsterdam, The Netherlands

[10] Department of Physics and Electrical Engineering, Linnaeus University, 351 95 Växjö, Sweden

[11] Institut für Theoretische Physik, Lehrstuhl IV: Weltraum und Astrophysik, Ruhr-Universität Bochum, D 44780 Bochum, Germany

[12] GRAPPA, Anton Pannekoek Institute for Astronomy and Institute of High-Energy Physics, University of Amsterdam, Science Park 904, 1098 XH Amsterdam, The Netherlands

[13] Institut für Astro- und Teilchenphysik, Leopold-Franzens-Universität Innsbruck, A-6020 Innsbruck, Austria

[14] School of Physical Sciences, University of Adelaide, Adelaide 5005, Australia

[15] LUTH, Observatoire de Paris, PSL Research University, CNRS, Université Paris Diderot, 5 Place Jules Janssen, 92190 Meudon, France

[16] Sorbonne Universités, UPMC Université Paris 06, Université Paris Diderot, Sorbonne Paris Cité, CNRS, Laboratoire de Physique Nu-

cléaire et de Hautes Energies (LPNHE), 4 place Jussieu, F-75252, Paris Cedex 5, France

[17] Laboratoire Univers et Particules de Montpellier, Université Montpellier, CNRS/IN2P3, CC 72, Place Eugène Bataillon, F-34095 Montpellier Cedex 5, France

[18] DSM/Irfu, CEA Saclay, F-91191 Gif-Sur-Yvette Cedex, France

[19] Astronomical Observatory, The University of Warsaw, Al. Ujazdowskie 4, 00-478 Warsaw, Poland

[20] Aix Marseille Université, CNRS/IN2P3, CPPM UMR 7346, 13288 Marseille, France

[21] Instytut Fizyki Jądrowej PAN, ul. Radzikowskiego 152, 31-342 Kraków, Poland

[22] Funded by EU FP7 Marie Curie, grant agreement No. PIEF-GA-2012-332350,

[23] School of Physics, University of the Witwatersrand, 1 Jan Smuts Avenue, Braamfontein, Johannesburg, 2050 South Africa

[24] Laboratoire d'Annecy-le-Vieux de Physique des Particules, Université Savoie Mont-Blanc, CNRS/IN2P3, F-74941 Annecy-le-Vieux, France

[25] Landessternwarte, Universität Heidelberg, Königstuhl, D 69117 Heidelberg, Germany

[26] Université Bordeaux, CNRS/IN2P3, Centre d'Études Nucléaires de Bordeaux Gradignan, 33175 Gradignan, France

[27] Oskar Klein Centre, Department of Physics, Stockholm University, Albanova University Center, SE-10691 Stockholm, Sweden

[28] Wallenberg Academy Fellow,

[29] Institut für Astronomie und Astrophysik, Universität Tübingen, Sand 1, D 72076 Tübingen, Germany

[30] Laboratoire Leprince-Ringuet, Ecole Polytechnique, CNRS/IN2P3, F-91128 Palaiseau, France

[31] APC, AstroParticule et Cosmologie, Université Paris Diderot, CNRS/IN2P3, CEA/Irfu, Observatoire de Paris, Sorbonne Paris Cité, 10, rue Alice Domon et Léonie Duquet, 75205 Paris Cedex 13, France

[32] Univ. Grenoble Alpes, IPAG, F-38000 Grenoble, France
CNRS, IPAG, F-38000 Grenoble, France

[33] Department of Physics and Astronomy, The University of Leicester, University Road, Leicester, LE1 7RH, United Kingdom

[34] Nicolaus Copernicus Astronomical Center, Polish Academy of Sciences, ul. Bartycka 18, 00-716 Warsaw, Poland

[35] Institut für Physik und Astronomie, Universität Potsdam, Karl-Liebknecht-Strasse 24/25, D 14476 Potsdam, Germany

[36] Friedrich-Alexander-Universität Erlangen-Nürnberg, Erlangen Centre for Astroparticle Physics, Erwin-Rommel-Str. 1, D 91058 Erlangen, Germany

[37] DESY, D-15738 Zeuthen, Germany

[38] Obserwatorium Astronomiczne, Uniwersytet Jagielloński, ul. Orla 171, 30-244 Kraków, Poland

[39] Centre for Astronomy, Faculty of Physics, Astronomy and Informatics, Nicolaus Copernicus University, Grudziadzka 5, 87-100 Torun, Poland

[40] Department of Physics, University of the Free State, PO Box 339, Bloemfontein 9300, South Africa

[41] Heisenberg Fellow (DFG), ITA Universität Heidelberg, Germany

[42] GRAPPA, Institute of High-Energy Physics, University of Amsterdam, Science Park 904, 1098 XH Amsterdam, The Netherlands

[43] Department of Physics, Rikkyo University, 3-34-1 Nishi-Ikebukuro, Toshima-ku, Tokyo 171-8501, Japan

[44] Japan Aerpspace Exploration Agency (JAXA), Institute of Space and Astronautical Science (ISAS), 3-1-1 Yoshinodai, Chuo-ku, Sagamihara, Kanagawa 229-8510, Japan

[45] Now at Santa Cruz Institute for Particle Physics and Department of Physics, University of California at Santa Cruz, Santa Cruz, CA 95064, USA

Appendix A: Spectral Points and Region Definitions

List of Objects

region	RA [deg]	Dec [deg]	R_1 [deg]	R_2 [deg]	ϕ_1 [deg]	ϕ_2 [deg]	area [deg^2]
whole SNR	133.00	−46.37	0.0	1.0	0	360	3.14
NW rim	133.10	−46.30	0.6	1.0	220	40	1.01
0	133.00	−46.37	0.0	0.6	0	360	1.13
1	133.00	−46.37	0.6	1.0	0	60	0.335
2	133.00	−46.37	0.6	1.0	60	120	0.335
3	133.00	−46.37	0.6	1.0	120	180	0.335
4	133.00	−46.37	0.6	1.0	180	240	0.335
5	133.00	−46.37	0.6	1.0	240	300	0.335
6	133.00	−46.37	0.6	1.0	300	360	0.335
A (point-like)	133.90	−46.74	0.0	$\sqrt{0.0125}$	0	360	0.0393
B	133.85	−46.65	0.0	0.3	0	360	0.283
C	133.50	−46.75	0.0	0.6	0	360	1.13
D (point-like)	133.25	−47.15	0.0	$\sqrt{0.0125}$	0	360	0.0393
B′			$B' = B \setminus A$				0.243
C′			$C' = C \setminus B \setminus D$				0.809

Table A.1. Region definitions used for the analysis of RX J0852.0−4622 specified with the following parameters of an annular region: the center coordinates in (RA, Dec, J2000), the inner and outer radii (R_1 and R_2 respectively) and the starting and ending polar angles (ϕ_1 and ϕ_2 respectively). The polar angles are defined in a similar way as the azimuthal angles in Fig. 2: starting at the 12 o'clock position (the North) and increasing anti-clockwise. The complex regions B′ and C′ are defined in terms of simple regions. In addition, the area of the sky covered by the corresponding region is also given.

E [TeV]	dΦ/dE [cm^{-2}s^{-1}TeV^{-1}]	excess	sign
0.407	$\left(1.23^{+0.28\text{stat}}_{-0.28\text{stat}} \pm 0.42_\text{syst}\right)10^{-10}$	329	4.4σ
0.571	$\left(8.32^{+0.76\text{stat}}_{-0.76\text{stat}} \pm 2.23_\text{syst}\right)10^{-11}$	1240	11σ
0.826	$\left(3.85^{+0.31\text{stat}}_{-0.31\text{stat}} \pm 0.95_\text{syst}\right)10^{-11}$	1230	13σ
1.21	$\left(1.85^{+0.14\text{stat}}_{-0.14\text{stat}} \pm 0.41_\text{syst}\right)10^{-11}$	1030	14σ
1.78	$\left(9.06^{+0.63\text{stat}}_{-0.62\text{stat}} \pm 1.90_\text{syst}\right)10^{-12}$	880	15σ
2.60	$\left(4.05^{+0.31\text{stat}}_{-0.31\text{stat}} \pm 0.85_\text{syst}\right)10^{-12}$	666	13σ
3.80	$\left(1.50^{+0.15\text{stat}}_{-0.15\text{stat}} \pm 0.33_\text{syst}\right)10^{-12}$	391	10σ
5.55	$\left(5.69^{+0.65\text{stat}}_{-0.65\text{stat}} \pm 1.31_\text{syst}\right)10^{-13}$	216	8.9σ
8.13	$\left(2.37^{+0.33\text{stat}}_{-0.32\text{stat}} \pm 0.53_\text{syst}\right)10^{-13}$	136	7.4σ
11.9	$\left(6.47^{+1.54\text{stat}}_{-1.51\text{stat}} \pm 1.41_\text{syst}\right)10^{-14}$	59	4.3σ
17.3	$\left(1.35^{+0.69\text{stat}}_{-0.68\text{stat}} \pm 0.33_\text{syst}\right)10^{-14}$	20	2.0σ
25.0	$\left(3.33^{+2.74\text{stat}}_{-2.69\text{stat}} \pm 1.20_\text{syst}\right)10^{-15}$	8	1.2σ

Table A.2. H.E.S.S. flux points for the spectrum of RX J0852.0−4622. The table shows the energy E, the differential flux dΦ/dE with 1σ statistical and systematic uncertainties, the excess and the significance of the point in number of Gaussian standard deviations σ.